Research Article Vol. 39, No. 12 / December 2022 / Journal of the Optical Society of America A C161

Journal of the Optical Society of America A
OPTICS, IMAGE SCIENCE, AND VISION

Generation of volumetrically full Poincaré beams

A. Nicholas Black[1,*] and Robert W. Boyd[1,2]

[1]Department of Physics and Astronomy, University of Rochester, 500 Wilson Blvd., Rochester, New York 14620, USA
[2]Department of Physics, University of Ottawa, 25 Templeton St., Ottawa, Ontario K1N 6N5, Canada
*Corresponding author: ablack18@ur.rochester.edu

Received 17 August 2022; revised 2 November 2022; accepted 11 November 2022; posted 14 November 2022; published 30 November 2022

Optical communications, remote sensing, particle trapping, and high-resolution imaging are a few research areas that benefit from new techniques to generate structured light. We present a method of generating polarization-structured laser beams that contain both full and partial polarization states. We demonstrate this method by generating an optical beam that contains every state of partial and full polarization. We refer to this beam as a *volumetrically full* Poincaré beam to distinguish it from full Poincaré beams, which contain all states of full polarization only. In contrast to methods relying upon spatial coherence to generate polarization-structured beams with partial polarization, our method creates well-collimated beams by relying upon temporal coherence.

https://doi.org/10.1364/JOSAA.473363

1. INTRODUCTION

Laser beams with spatially varying amplitude, phase, or polarization beyond that of a uniformly polarized Gaussian beam have garnered a significant amount of attention over the last few decades and are generically referred to as structured light [1,2]. Many of the most common amplitude-structured beams are orthonormal solutions to the scalar paraxial wave equation, making them suitable as an encoding basis in optical communications [3,4]. Furthermore, the infinite-dimensional Hilbert space formed by orthonormal solutions to the paraxial wave equation allows for an increased channel capacity per photon [5] compared to binary encoding schemes, such as polarization. Beams with a spatially varying polarization can also be used as an encoding basis with a mathematical similarity to the Poincaré sphere formalism but generalized to higher dimensions [6,7]. Because the polarization structure of these beams may vary in all three spatial dimensions, it is possible to form knotted polarization topologies that can also be used as an encoding basis [8]. Polarization-structured beams have also received attention for their resistance to beam breakup resulting from turbulence and/or nonlinear self-focusing [9–11]. Additionally, it has been demonstrated that radially polarized beams can achieve a tighter focus [12], potentially increasing the precision of laser trapping [13] and increasing the resolution in confocal microscopy [14].

Fully polarized beams, such as full Poincaré (FP) and vector vortex (VV) beams, have been the subject of many studies in the optics community. FP beams [15,16] contain every polarization state on the surface of the Poincaré sphere, while VV [17] beams contain states along a path on the surface of the Poincaré sphere. Other types of polarization-structured beams that include states of partial and full polarization have also been reported previously [18–23]. One such example that is spatially coherent and contains every polarization state on the surface and interior of the Poincaré sphere was developed by Beckley *et al.*, referred to here as volumetrically FP (VFP) beams [18]. In this paper, we present a method of generating polarization-structured beams comprising at most two temporally incoherent beams of opposite orbital angular momenta or of a relative inversion about the horizontal axis and use it to generate a VFP beam. Furthermore, the degree of temporal coherence between the two constituent beams can be varied continuously from fully coherent to fully incoherent. In partially coherent polarization-structured beams generated from Gaussian Schell-model sources, the degree of polarization is intrinsically coupled to the Rayleigh range of the source [24]. By utilizing temporal coherence rather than spatial coherence to control the degree of polarization, the beams generated in our system can remain well collimated upon propagation for varying degrees of temporal coherence. Our results and methods add to the quickly growing field of structured light generation [25–31] and may have an impact on studies of what has been called "classical entanglement" [32] and beam dynamics in complex and nonlinear media.

2. BACKGROUND

A VFP beam comprises an incoherent superposition of two FP beams of opposite orbital angular momenta [18]:

$$\mathbf{VFP}(\rho, \theta, z) = a_1 \mathbf{FP}_{+}(\rho, \theta, z) + a_2 \mathbf{FP}_{-}(\rho, \theta, z), \quad (1)$$

where

$$\mathbf{FP}_{\pm}(\rho, \theta, z) = \mathrm{LG}_{0,0}(\rho, \theta, z)\mathbf{e}_{\mathrm{L}} + \mathrm{LG}_{0,\pm 1}(\rho, \theta, z)\mathbf{e}_{\mathrm{R}}. \quad (2)$$

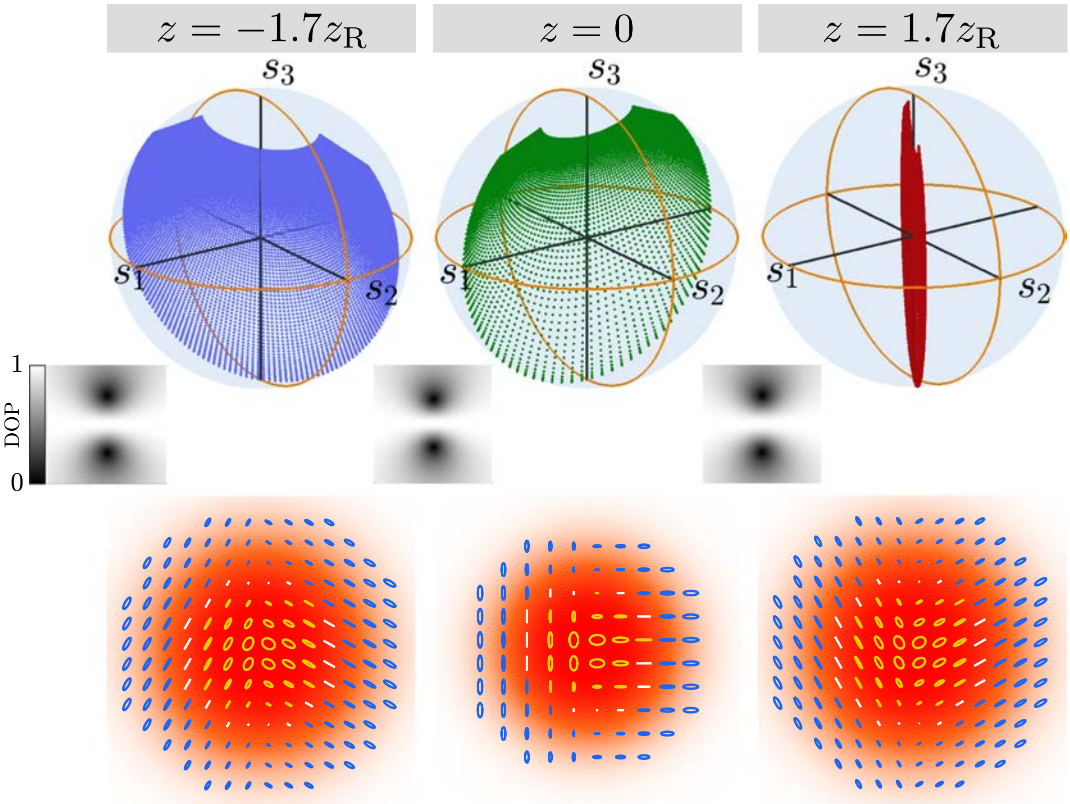

Fig. 1. Poincaré sphere coverage (top row) and transverse polarization structure (bottom row) of a VFP beam at three positions along the beam's propagation axis. Inset between the Poincaré sphere coverage and the polarization structure is the spatially resolved degree of polarization (DOP) for each location. (top row) As the beam propagates, the polarization states present in the beam form a disk-like surface in the Poincaré sphere that rotates about the s_3 axis. (bottom row) The transverse polarization structure of the VFP beam contains varying degrees of polarization, as indicated by the relative size of the polarization ellipses plotted at various locations on top of the beam's transverse intensity structure (orange). Yellow, blue, and white ellipses indicate left-circular, right-circular, and linear polarizations, respectively. Upon propagation, the local polarization at a point in the beam undergoes a rotation. Beam sizes are scaled differently to aid visual inspection.

Coefficients a_1 and a_2 in Eq. (1) are uncorrelated stocastic variables of equal amplitude. That is, $\langle a_1 a_2^* \rangle = \langle a_2 a_1^* \rangle = 0$ and $\langle |a_1|^2 \rangle = \langle |a_2|^2 \rangle$, where brackets denote an average over the exposure time of the camera that records the beam profile. Equation (2) shows that FP beams comprise two orthogonally polarized Laguerre–Gauss modes ($LG_{p,l}$) with an azimuthal index, l, differing by one. Depending upon the sign of the azimuthal index, FP beams can have a "lemon" ($l = +1$) or a "star" ($l = -1$) polarization topology. For the sake of simplicity, we have ignored any phase difference between the beams on the R.H.S of Eq. (2), but such a phase difference would impart a rigid rotation to the polarization structure [15]. Unit vectors $\mathbf{e}_L$ and $\mathbf{e}_R$ denote left- and right-circular polarization, respectively. The Stokes parameters' dependence upon cylindrical coordinates ρ, θ, and z reveals how every polarization state is present at some location in the VFP beam [18]:

$$s_0 = |LG_{0,0}|^2 \left[1 + \tilde{\rho}^2\right],$$
$$\frac{s_1}{s_0} = \frac{2\tilde{\rho}}{(1+\tilde{\rho}^2)} \cos\theta \cos\theta_G(z),$$
$$\frac{s_2}{s_0} = \frac{-2\tilde{\rho}}{(1+\tilde{\rho}^2)} \cos\theta \sin\theta_G(z),$$
$$\frac{s_3}{s_0} = \frac{\tilde{\rho}^2 - 1}{1+\tilde{\rho}^2}, \tag{3}$$

where $\tilde{\rho} = \sqrt{2}\rho/w(z)$, $w(z)$ is the beam radius, and $\theta_G(z)$ is the Gouy phase [33] of the $LG_{0,0}$ beam. Aside from the dependence upon $\theta_G(z)$, Eq. (3) represents parametric equations of a unit disk whose diameter lies along the s_3 axis of the Poincaré sphere. As the Gouy phase changes, the disk rotates about the s_3 axis, eventually sweeping the entire volume of the Poincaré sphere. Because the Gouy phase depends upon z as $-\arctan(z/z_R)$, where z_R is the Rayleigh range, half of the disk's rotation occurs within $\pm z_R$. The full π rotation of the disk occurs only for propagation from $z = -\infty$ to $z = +\infty$.

Figure 1 shows the Poincaré sphere coverage and transverse polarization structure of the VFP beam at three locations along the beam's propagation: $z = -1.7z_R$, $z = 0$, and $z = 1.7z_R$.

In each plane of constant z, there are two regions where the degree of polarization is zero. These correspond to areas where the polarizations of the constituent FP beams are orthogonal. Full polarization occurs in regions where the polarizations of the constituent FP beams are the same [34]. Areas of partial polarization in the VFP beam result from the polarizations of the two FP beams being not completely parallel or orthogonal. Individually, the polarization structures of the constituent FP beams rotate due to the difference in the Gouy phases of the $LG_{0,0}$ and $LG_{0,\pm 1}$ beams that they are made from. This fact, coupled with the smooth transition between regions of parallel polarizations and orthogonal polarizations in the constituent FP beams, allows the VFP beam to contain every Poincaré sphere state. We also draw attention to the seemingly abrupt change from vertical to horizontal elliptical polarization at the center of the beam in the horizontal direction at $z = 0$. Along the horizontal axis, the constituent FP beams have the same polarization. Along the vertical axis, the linear component of the constituent FP beams' polarization is orthogonal. Between these axes, the polarizations of the constituent FP beams experience a smooth transition from the same polarization to having orthogonal linear components of polarization. The net result of these effects is that the polarization ellipses in the VFP beam are in the same direction on either side of the vertical axis of the beam. Outside of regions of zero polarization, the polarization along the vertical axis of the VFP beam is perfectly circularly polarized, though with a varying degree of polarization due to the varying presence of orthogonal linear polarization components of the constituent FP beams. In other words, the vertical axis is a c-line. The behavior is also present in the $z = -1.7z_R$ and $z = 1.7z_R$ profiles.

The lack of states at the top of the Poincaré sphere is fundamentally related to the fact that states at the north pole of the Poincaré sphere are located infinitely far from the beam's propagation axis. Geometrically, FP beams are a stereographic projection of the Poincaré sphere to an infinite plane [15], placing the northernmost Poincaré sphere states at infinity. However, the finite numerical precision of the VFP beam's representation in the computer coupled with the finite window size chosen in Fig. 1 also limits the amount of states plotted at the top of the Poincaré sphere. We note that methods to generate finite FP beams have been demonstrated theoretically and experimentally [35,36]. The disk-like surface of Poincaré sphere states in Fig. 1 rotates from approximately $-59.53°$ at $z = -1.7z_R$ to $59.53°$ at $z = 1.7z_R$. Thus, a majority of Poincaré sphere states are present within several Rayleigh ranges of the beam waist.

3. EXPERIMENT

The experimental setup for generating a VFP beam is shown in Fig. 2. In the "coherence control system" stage, a 780 nm tunable diode laser (Toptica DL pro 780) is coupled into a phase-shifting electro-optic modulator (EOM) via a polarization-maintaining fiber (PMF). The EOM is driven with amplified white noise with a bandwidth of ∼1 GHz and an amplitude of 39 dBm. For the EOM used in Fig. 2 (AdvR WPM-K0780-P85P85ALO), 39 dBm corresponds to a phase shift of $\sim 6.5\pi$. Maximum phase shift values lower than 6π were found to yield an incomplete broadening of the laser's bandwidth. The use of phase-only devices to broaden a laser's linewidth is described in more detail in Ref. [37]. The beam is then coupled into a tapered amplifier (TA) with a flat gain profile over the bandwidth of the beam (Toptica BoosTA). The spectrum of the beam is measured after

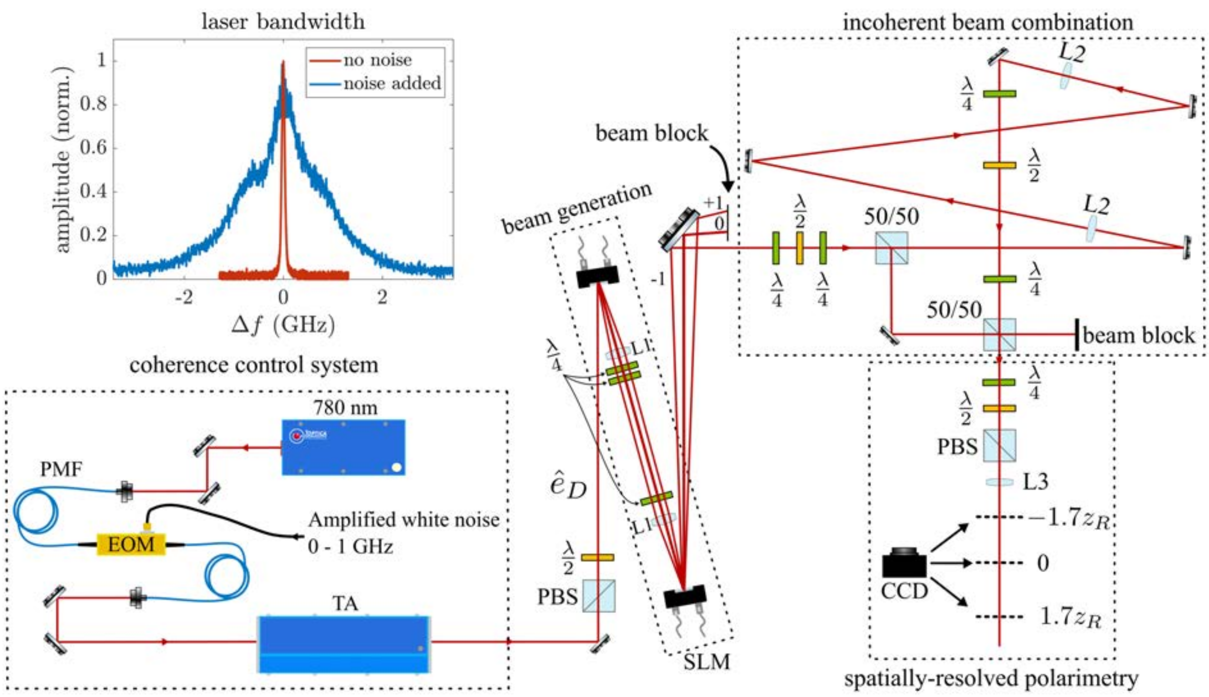

Fig. 2. Experimental setup for generating a VFP beam. 780 nm, tunable diode laser; PMF, polarization-maintaining fiber; EOM, phase-shifting electro-optic modulator; TA, tapered amplifier; PBS, polarizing beam splitter; $\lambda/2$, half-wave plate; SLM, spatial light modulator; L1, $f = 20$ cm lens; $\lambda/4$, quarter-wave plate; 50/50, 50/50 beam splitter; L2, $f = 2.5$ m lens; L3, $f = 1$ m lens; CCD, camera.

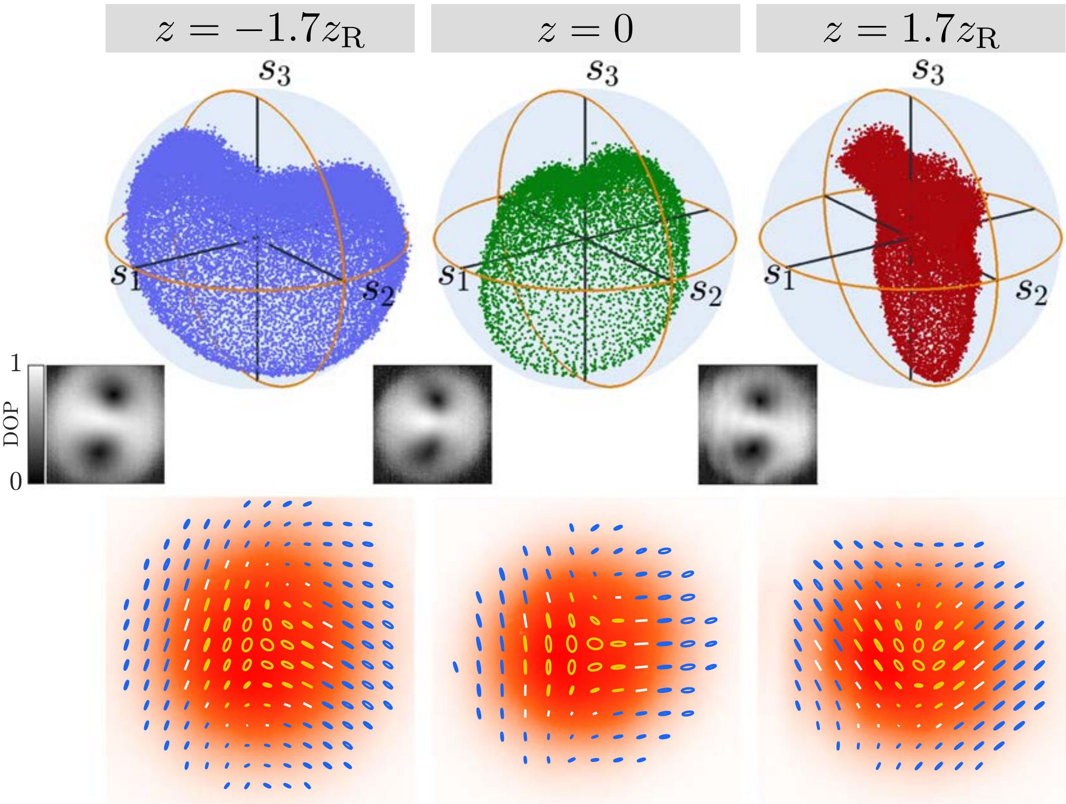

Fig. 3. Experimentally measured Poincaré sphere coverage (top row) and transverse polarization structure (bottom row) of a VFP beam. The middle row shows the degree of polarization across the transverse extent of the beam. Generally, the experimental results are in close agreement with the theoretical results of Fig. 1.

the TA with and without noise (upper-left inset) using a scanning Fabry–Perot interferometer (FPI) (Thorlabs SA210-5B), confirming the broadening of the spectrum from the added phase noise. With no phase noise added, the measured bandwidth corresponds to the resolution of the FPI (67 MHz). In the "beam generation" stage, the beam's polarization is rotated to diagonal before reflecting from two spatial light modulators (SLMs) with coinciding image planes [27].

The polarization is rotated and carefully controlled by three quarter-wave plates ($\lambda/4$) between the two SLMs such that each SLM acts on a different orthogonal linear polarization. The SLMs are programmed with computer-generated holograms [26] such that the beam produced on the -1 diffractive order is $\mathrm{LG}_{0,0}\mathbf{e}_\mathrm{V} + \mathrm{LG}_{0,1}\mathbf{e}_\mathrm{H}$. Because both polarization components copropagate through the optical system, this method of beam generation is inherently phase stable. In the "incoherent beam combination" stage, the polarization components of the generated beam are transformed to the circular basis to produce an FP_+ beam with the polarization of the two constituent modes exchanged before the beam is split into two paths by a 50/50 beam splitter. A quarter/half/quarter series of wave plates is used rather than a single quarter-wave plate because it offers greater control over the resulting polarization states. The transmitted path consists of a 10 m imaging delay line with an even number of reflections and a series of quarter-wave and half-wave plates to correct for polarization rotations induced by the dielectric mirrors. The FP beam that was reflected from the first 50/50 beam splitter experiences an odd number of reflections, reversing its orbital angular momentum relative to the transmitted FP beam. The two FP beams are then recombined at a second 50/50 beam splitter. The 10 m freespace delay between the two beams ensures that they combine incoherently since the coherence length of the beams is ~95.4 mm. After recombination, the beam travels through a quarter-wave plate, a half-wave plate, a polarizing beam splitter, and an $f = 1$ m lens to perform spatially resolved polarimetry at three longitudinal positions around the beam waist: $z = -1.7z_\mathrm{R}$, $z = 0$, and $z = 1.7z_\mathrm{R}$. The full-width at half max of the beam at $z = -1.7z_\mathrm{R}$, $z = 0$, and $z = 1.7z_\mathrm{R}$ is approximately 0.66(2) mm, 0.33(2) mm, and 0.62(2) mm, respectively. The camera used to record the spatially resolved polarimetry results (Gentec-EO Beamage-4M) has a pixel size of 5.5 µm.

4. RESULTS

Figure 3 shows the results of generating a VFP beam with the setup in Fig. 2. The experimentally generated VFP beam agrees closely with the ideal theoretical VFP beam shown in Fig. 1. At positions $z = -1.7z_\mathrm{R}$ and $z = 1.7z_\mathrm{R}$, approximately 40,000 pixels were used to create the Poincaré sphere coverage. At $z = 0$, approximately 15,000 pixels were used to create the Poincaré sphere coverage. Like an ideal VFP beam, the Poincaré sphere coverage is a disk-like surface that rotates about the s_3 axis. However, the Poincaré sphere coverage for the experimentally generated VFP beam is a surface with nonzero thickness in each plane. The deviation from an ideal thickness of zero is primarily due to the imperfect retardation of the quarter- and half-wave plates that control the polarization. The lack of states near the positive s_3 pole of the surface can be attributed to finite sensor size and bit depth of the camera. That is to say, pure right-circular polarization is present only far from the center of the beam, where the intensity is low and the edges of the camera sensor are located. The low signal-to-noise ratio far from the center of the beam is responsible for the increased noise present near the s_3 pole. The rotation angle of the surface at each longitudinal position is estimated using maximum likelihood (ML) fitting with the model of a plane containing the s_3 axis and one free parameter describing the angle of the plane relative to the s_1 axis. Monte Carlo simulation was used to determine the uncertainty in the fits. ML fitting returns the following values of the rotation angle for $z = -1.7z_R$, 0, and $1.7z_R$, respectively: $\phi = -44.03(1)°, 12.03(3)°, 59.58(1)°$. Ideally, the angle of the disk-like surface at $z = -1.7z_R$, 0, and $1.7z$R should be approximately $-59.53°$, 0°, and 59.53°, respectively. The difference between the ideal VFP beam and the experimental results can be primarily attributed to the wave plates used to control and measure the polarization, as well as the uncertainty in the exact location of the beam waist.

5. CONCLUSION

We have demonstrated an optical system capable of producing fully and partially polarized beams with varying amounts of temporal coherence. Using this system, we generated a VFP beam for the first time, to our knowledge. While past reports of VFP beam generation have relied upon the incoherent addition of polarimetry data taken sequentially from two FP beams of opposite orbital angular momenta [18], our method produces a VFP beam available in real time. With minimal reconfiguration (amounting to blocking beams), our system can generate any arbitrary fully polarized polarization-structured beam with varying amounts of temporal coherence. Furthermore, this system can be used to generate beams that consist of either a coherent or an incoherent superposition of polarization-structured beams of opposite orbital angular momenta or a relative inversion about the horizontal axis, though phase stabilization would be necessary for a coherent combination. Our results add a method of generating polarization-structured beams with regions containing varying degrees of polarization to the quickly growing toolbox of structured light generation. It may be possible to generate a VFP beam using spatially, rather than temporally, incoherent light, but the Rayleigh range of such a beam will depend upon the transverse coherence length. Polarization-structured beams such as the VFP beam generated in our experiment will continue to advance the fields of imaging, nonlinear optics, and communications.

Funding. Office of Naval Research (N00014-19-1-2247, N00014-20-1-2558); Natural Sciences and Engineering Research Council of Canada; Canada Research Chairs program.

Disclosures. The authors declare no conflicts of interest.

Data availability. Data underlying the results presented in this paper are not publicly available at this time but may be obtained from the authors upon reasonable request.

REFERENCES

1. H. Rubinsztein-Dunlop, A. Forbes, M. V. Berry, *et al.*, "Roadmap on structured light," J. Opt. **19**, 013001 (2016).
2. A. Forbes, "Structured light from lasers," Laser Photon. Rev. **13**, 1900140 (2019).
3. G. Gibson, J. Courtial, M. J. Padgett, M. Vasnetsov, V. Pas'ko, S. M. Barnett, and S. Franke-Arnold, "Free-space information transfer using light beams carrying orbital angular momentum," Opt. Express **12**, 5448–5456 (2004).
4. G. Molina-Terriza, J. P. Torres, and L. Torner, "Twisted photons," Nat. Phys. **3**, 305–310 (2007).
5. M. Mirhosseini, O. S. Magaña-Loaiza, M. N. O'Sullivan, B. Rodenburg, M. Malik, M. P. J. Lavery, M. J. Padgett, D. J. Gauthier, and R. W. Boyd, "High-dimensional quantum cryptography with twisted light," New J. Phys. **17**, 033033 (2015).
6. G. Milione, H. I. Sztul, D. A. Nolan, and R. R. Alfano, "Higher-order Poincaré sphere, Stokes parameters, and the angular momentum of light," Phys. Rev. Lett. **107**, 053601 (2011).
7. A. Sit, F. Bouchard, R. Fickler, J. Gagnon-Bischoff, H. Larocque, K. Heshami, D. Elser, C. Peuntinger, K. Günthner, B. Heim, C. Marquardt, G. Leuchs, R. W. Boyd, and E. Karimi, "High-dimensional intracity quantum cryptography with structured photons," Optica **4**, 1006–1010 (2017).
8. H. Larocque, A. D'Errico, M. F. Ferrer-Garcia, A. Carmi, E. Cohen, and E. Karimi, "Optical framed knots as information carriers," Nat. Commun. **11**, 5119 (2020).
9. Y. Gu, O. Korotkova, and G. Gbur, "Scintillation of nonuniformly polarized beams in atmospheric turbulence," Opt. Lett. **34**, 2261–2263 (2009).
10. S.-M. Li, Y. Li, X.-L. Wang, L.-J. Kong, K. Lou, C. Tu, Y. Tian, and H.-T. Wang, "Taming the collapse of optical fields," Sci. Rep. **2**, 1007 (2012).
11. F. Bouchard, H. Larocque, A. M. Yao, C. Travis, I. De Leon, A. Rubano, E. Karimi, G.-L. Oppo, and R. W. Boyd, "Polarization shaping for control of nonlinear propagation," Phys. Rev. Lett. **117**, 233903 (2016).
12. R. Dorn, S. Quabis, and G. Leuchs, "Sharper focus for a radially polarized light beam," Phys. Rev. Lett. **91**, 233901 (2003).
13. J.-B. Béguin, J. Laurat, X. Luan, A. P. Burgers, Z. Qin, and H. J. Kimble, "Reduced volume and reflection for bright optical tweezers with radial Laguerre-Gauss beams," Proc. Natl. Acad. Sci. USA **117**, 26109–26117 (2020).
14. W. T. Tang, E. Y. S. Yew, and C. J. R. Sheppard, "Polarization conversion in confocal microscopy with radially polarized illumination," Opt. Lett. **34**, 2147–2149 (2009).
15. A. M. Beckley, T. G. Brown, and M. A. Alonso, "Full Poincaré beams," Opt. Express **18**, 10777–10785 (2010).
16. E. J. Galvez, S. Khadka, W. H. Schubert, and S. Nomoto, "Poincaré-beam patterns produced by nonseparable superpositions of Laguerre–Gauss and polarization modes of light," Appl. Opt. **51**, 2925–2934 (2012).
17. Q. Zhan, "Cylindrical vector beams: from mathematical concepts to applications," Adv. Opt. Photon. **1**, 1–57 (2009).
18. A. M. Beckley, T. G. Brown, and M. A. Alonso, "Full Poincaré beams ii: partial polarization," Opt. Express **20**, 9357–9362 (2012).
19. L. Guo, Y. Chen, X. Liu, L. Liu, and Y. Cai, "Vortex phase-induced changes of the statistical properties of a partially coherent radially polarized beam," Opt. Express **24**, 13714–13728 (2016).
20. J. Zeng, C. Liang, H. Wang, F. Wang, C. Zhao, G. Gbur, and Y. Cai, "Partially coherent radially polarized fractional vortex beam," Opt. Express **28**, 11493–11513 (2020).
21. S. Joshi, S. N. Khan, P. Senthilkumaran, and B. Kanseri, "Coherence-induced polarization effects in vector vortex beams," Opt. Lett. **45**, 4815–4818 (2020).
22. T. Li, D. Li, X. Zhang, K. Huang, and X. Lu, "Partially coherent radially polarized circular Airy beam," Opt. Lett. **45**, 4547–4550 (2020).
23. S. Joshi, S. N. Khan, B. Kanseri, and P. Senthilkumaran, "Investigation of partially coherent vector vortex beams with non-isotropic states of spatial correlation," Opt. Express **30**, 32230–32243 (2022).
24. G. Gbur and E. Wolf, "The Rayleigh range of Gaussian Schell-model beams," J. Mod. Opt. **48**, 1735–1741 (2001).

25. L. Marrucci, C. Manzo, and D. Paparo, “Optical spin-to-orbital angular momentum conversion in inhomogeneous anisotropic media,” Phys. Rev. Lett. **96**, 163905 (2006).
26. V. Arrizón, U. Ruiz, R. Carrada, and L. A. González, “Pixelated phase computer holograms for the accurate encoding of scalar complex fields,” J. Opt. Soc. Am. A: **24**, 3500–3507 (2007).
27. B. Khajavi and E. J. Galvez, “Preparation of Poincaré beams with a same-path polarization/spatial-mode interferometer,” Opt. Eng. **54**, 111305 (2015).
28. J. Jia, K. Zhang, G. Hu, M. Hu, T. Tong, Q. Mu, H. Gao, F. Li, C.-W. Qiu, and P. Zhang, “Arbitrary cylindrical vector beam generation enabled by polarization-selective Gouy phase shifter,” Photon. Res. **9**, 1048–1054 (2021).
29. J. Qi, W. Wang, B. Shi, H. Zhang, Y. Shen, H. Deng, W. Pu, X. Liu, H. Shan, X. Ma, L. Zhang, W. Lu, M. Fu, and X. Li, “Concise and efficient direct-view generation of arbitrary cylindrical vector beams by a vortex half-wave plate,” Photon. Res. **9**, 803–813 (2021).
30. M. Wang, G. Hu, S. Chand, M. Cotrufo, Y. Abate, K. Watanabe, T. Taniguchi, G. Grosso, C.-W. Qiu, and A. Alù, “Spin-orbit-locked hyperbolic polariton vortices carrying reconfigurable topological charges,” eLight **2**, 12 (2022).
31. A. H. Dorrah and F. Capasso, “Tunable structured light with flat optics,” Science **376**, eabi68 (2022).
32. J. H. Eberly, X.-F. Qian, A. A. Qasimi, H. Ali, M. A. Alonso, R. Gutiérrez-Cuevas, B. J. Little, J. C. Howell, T. Malhotra, and A. N. Vamivakas, “Quantum and classical optics–emerging links,” Phys. Scr. **91**, 063003 (2016).
33. R. W. Boyd, “Intuitive explanation of the phase anomaly of focused light beams,” J. Opt. Soc. Am. **70**, 877–880 (1980).
34. M. Born and E. Wolf, *Principles of Optics: 60th Anniversary Edition*, 7th ed. (Cambridge University, 2019), pp. 619–632.
35. G. Arora, S. K. Pal, and P. Senthilkumaran, “Full Poincaré beam delineation based on the Stokes vortex ring,” J. Opt. **23**, 105201 (2021).
36. B. Radhakrishna, G. Kadiri, and G. Raghavan, “Polarimetric method of generating full Poincaré beams within a finite extent,” J. Opt. Soc. Am. A **39**, 662–666 (2022).
37. J. M. Wheeler, J. N. Chamoun, and M. J. F. Digonnet, “Optimizing coherence suppression in a laser broadened by phase modulation with noise,” J. Lightwave Technol. **39**, 2994–3001 (2021).